

Localized manipulation of martensite transformation in double-sided incremental forming by varying the deformation path

by

Shayan Darzi¹, Enrico Tulung², Brad L. Kinsey¹, Jinjin Ha^{1*}

*Corresponding author: jinjin.ha@unh.edu

June 2024

¹ Department of Mechanical Engineering, University of New Hampshire, Durham, NH 03824, USA

² Department of Chemical Engineering, University of New Hampshire, Durham, NH 03824, USA

Abstract

Incremental sheet metal forming is known for its high flexibility, making it suitable for fabricating low-batch, highly customized complex parts. In this paper, a localized multi-pass toolpath referred to as localized reforming, with reverse forming in a region of interest, is employed within the double-sided incremental forming (DSIF) process to manipulate the mechanical properties of a truncated pyramid formed from austenitic stainless steel sheet, SS304, through deformation-induced martensite transformation. DSIF forms a clamped sheet through localized deformations by two opposing tools. The toolpath effect in localized reforming is examined in terms of martensite transformation, geometrical accuracy, and thickness distribution. The results are compared with a conventional toolpath, i.e., forming in a single pass. The results show that varying toolpaths leads to different martensite transformation levels, while final geometry and thickness remain similar. The study demonstrates that localized reforming significantly increases martensite transformation in the specified region, i.e., the center of the pyramid wall, to ~70%, with a martensite fraction remaining around 25% elsewhere. In comparison, using a single pass forming toolpath leads to a decreasing martensite fraction from the base of the pyramid towards the apex, due to the heat generated, with values <10% along the entire wall. Through finite element simulation, it is shown that the increase in martensite transformation of the region of interest is with the plastic deformation accumulation during the reverse pass. These findings highlight the potential to tailor mechanical properties in specific areas using a reforming toolpath in DSIF.

Keywords: Incremental sheet forming, reforming toolpath, deformation-induced martensite transformation, stainless steel

Nomenclature:

α	Pyramid wall angle
β	Reverse pass wall angle
Н	Height of the reformed region of interest
L_{ref}	Length of the reformed region of interest
L_i	Half-length of the square base of the pyramid in the initial pass
l_i	Half-length of the square apex of the pyramid in the initial pass
L_r	Half-length of the square apex of the pyramid in the reverse
	pass
l_r	pass Half-length of the square, recessed area of the pyramid after
l_r	
l_r	Half-length of the square, recessed area of the pyramid after
	Half-length of the square, recessed area of the pyramid after the reverse pass
	Half-length of the square, recessed area of the pyramid after the reverse pass Half-length of the square apex of the pyramid in the target

1. Introduction

Incremental forming is a non-conventional sheet metal forming process in which one or more tools are used to locally form the sheet metal, which is clamped at its periphery, into its final geometry [1]. The most common type of incremental forming is single point incremental forming (SPIF), which employs a single, e.g., hemispherical, tool on one side of the sheet, as shown in Figure 1a. Unlike conventional sheet forming methods, incremental forming can create intricate geometries without dedicated dies like in stamping [2,3] while it presents superior formability beyond the conventional stretching-based evaluation method [4–6]. These unique characteristics make incremental forming an excellent choice for rapid prototyping sheet metal components [7] and applications with low-batch, highly customized production requirements in aviation [8], automotive [9,10], and biomedical industries [11].

Despite its numerous advantages, SPIF has certain limitations related to speed, geometric accuracy, and formability [12]. To address these constraints, researchers have studied various process parameters and their interactions [13]. Golabi and Khazaali [14] utilized SPIF to form a 0.5 mm thick SS304 sheet into a frustum, observing reduced formability when the vertical step was increased from 1 mm to 2 mm. Conversely, Darzi et al. [15] noted improved formability in SPIF when the vertical step was increased from 0.3 mm to 0.6 mm, employing a graphite powder lubricant to form a 1 mm thick AA6061 aluminum into a frustum target geometry.

In addition to optimizing process parameters, researchers have explored several variations of incremental forming to enhance its capabilities. These variants include two-point incremental forming (TPIF) [16] where a die is included in the process (as shown in Figure 1b), multi-point incremental forming (MPIF) [17], and double-sided incremental forming (DSIF) [18]. DSIF introduces a second tool, often referred to as

the support tool, which operates on the opposite side of the sheet metal, as shown in Figure 1c. This figure also summarizes the important process parameters in DSIF, e.g., wall angle, vertical step, initial thickness of the sheet, tool diameter, and thickness of the squeezed wall.

DSIF improves formability and geometric accuracy while still maintaining the dieless feature of SPIF [19]. The presence of the second tool in DSIF introduces a compressive deformation to stretching, bending, and shear deformations present in SPIF [20–22]. This stress combination enhances the formability and geometrical accuracy while maintaining the plastic deformation at the desired local region around tool-sheet contact [23].

The squeeze factor in DSIF, which is defined as the ratio of the tangential distance between the tip of the two hemispherical tools to the sheet metal thickness, increases hydrostatic pressure and lowers stress triaxiality due to the presence of the second tool in DSIF, which contributes to the increased formability [24,25]. Wang et al. [26] demonstrated that a higher squeeze factor and an overbending toolpath during the DSIF process led to reduced springback in AA7075 cone-shaped parts with an initial thickness of 1 mm. However, excessive supporting forces, which generate excessive squeezing pressure, can trigger localized thinning leading to early fracture of the material in the DSIF process [27].

Toolpath design is also an important process parameter affecting the incremental forming processes. Junchao et al. [28] successfully applied a multi-pass strategy in SPIF to form a complex DC04 car taillight bracket with an initial thickness of 0.8 mm. The normal single pass toolpath had failed, resulting in material rupture. They reported that increasing the number of passes led to reduced thinning in the formed part and a geometry that was closer to the desired shape. Moser et al. [29] increased the

maximum achievable wall angle from 61° to 82°, while forming an axisymmetric cylinder out of a 1mm thick AA5754-O sheet, by using a multi-pass toolpath in DSIF.

One of the unique advantages of the incremental forming process lies in its capability to control the deformation path, allowing for the customization of the mechanical properties of the final part through, e.g., deformation-induced α '-martensite transformation [30]. This martensite transformation involves a change in the crystal structure from face-centered cubic (fcc, γ -austenite) to hexagonal closed packed (hcp, ϵ -martensite), and finally to body-centered tetragonal (bct, α '-martensite), resulting in increased strength as the fraction of martensite increases.

Several important parameters can influence the deformation-induced martensitic transformation, such as chemical composition, plastic strain level [31], stress state [32–34], and temperature [30]. In the case of austenitic stainless steels, the attainable α'-martensite phase increases at higher strain levels and lower temperatures as reported for SS304L [34,35], SS304 [36], and SS316L [37–39]. Different chemical compositions exhibit varying degrees of transformation under different stress states.

The incremental forming process parameters that are adjustable to affect the α'martensite transformation include the toolpath, feedrate [40], external cooling
utilization, and stress superposition [41]. Darzi et al. [42] increased martensite volume
fraction from <10% to 95% along SS304L truncated pyramid walls, using DSIF. This
was achieved by using vortex tubes for cooling and a three-pass, reforming toolpath,
which generated higher strains while maintaining the same final geometry. Although
this study proved the concept of adjusted mechanical properties using DSIF, more
research is required to explore deformation mechanisms, especially related to varying
process parameters, and localized property manipulation in DSIF. This will be crucial
knowledge for producing, e.g., trauma-fixation hardware with heterogeneous

mechanical properties, like increasing strength at mounting points while preserving formability elsewhere.

In this study, the ability of the DSIF process is demonstrated to locally manipulate the deformation-induced martensite transformation within a SS304 sheet metal by varying the deformation path and feedrate. Localized reforming is performed with a reverse pass in the region of interest, which increases the martensite fraction to ~70%, while outside of the reforming area remains at ~25%. Moreover, the FE simulation is used to explain the effect of the reverse pass on plastic deformation and its relation to the martensite transformation. This research underscores the potential for customizing the local mechanical properties of the final part during the incremental forming while maintaining consistency in the final geometry and thickness distribution of the components.

2. Materials and methods

Experiments are conducted using the DSIF machine, depicted in Figure 2a. Square blanks, measuring 215 mm × 215 mm, are cut from a 1.2 mm thick austenitic stainless steel SS304 sheet using an abrasive waterjet cutting machine. The initial martensite fraction of the material is near zero. For the DSIF process, two hemispherical-tip tools made of A2 steel with a 10 mm diameter are employed. One tool performs forming (i.e., forming tool) while the other serves the role of supporting the sheet on the opposite side (i.e., support tool), as shown in Figure 2b.

A FLIR infrared (IR) thermal camera (SC-645) measures the temperature variations caused by plastic deformation and friction between the tools and the sheet. The camera has a resolution of 0.05°C, a temperature range of 20 to 650°C, and a spatial resolution of 640 × 480 pixels. The emissivity of the lubricated surface is

calibrated and determined to be 0.97 at 50°C, representing the average temperature during the IF process under different experimental cases in this study. Thermal image analysis is conducted using FLIR Research IR software, and images were captured at a rate of 1 Hz. The camera position in the setup is shown in Figure 2b.

The target geometry for the experiments is a truncated square pyramid with a 45° wall angle (α), a 90 mm square base ($2L_i$), and a 30 mm flat apex ($2l_f$), illustrated in Figure 3a. To enhance the deformation-induced martensite in the region of interest, i.e., the center of the pyramid wall, a localized reforming toolpath is employed. This deformation path consists of three passes: the initial pass, the reverse pass, and the final pass. The region of interest is defined as a section of the wall with a length of L_{ref} , centered at point C (red circle in Figure 3) and located at a height of H on the final part geometry (see Figure 3a).

In the initial pass, a truncated square pyramid with a wall angle of α , a square base of $2L_i$, and a flat apex square with a side of $2l_i$ is formed, in the positive z-direction. Then the part is inverted to perform the reverse pass in the opposite forming direction, i.e., negative z-direction, starting from point B (purple circle in Figure 3, located at the height h_r on the wall) with the wall angle of β with respect to the horizontal line ($\alpha + \beta$ with respect to the wall of the initial pass) and the apex square side of $2l_r$. Note that the dimensions of the reverse pass are calculated in a way to ensure that the length of the reformed wall remains as L_{ref} . In the final pass, the part is inverted once more to form the specimen to the final target geometry in the positive z-direction, i.e., the same forming direction as the initial pass. In this pass, tools start the deformation from point A (black circle in Figure 3), located at the height of h_f . This is done to compensate for any unintended deformation of the wall in the vicinity of point B (purple

circle in Figure 3) caused by the reverse pass. Parameters l_i , h_r , L_r , l_r , and h_f are calculated based on the following trigonometric equations:

$$l_i = L_i - H \cot \alpha - \frac{L_{ref}}{2} \cdot \cos \alpha \tag{1}$$

$$h_r = H - \frac{L_{ref}}{2} \cdot \sin \alpha \tag{2}$$

$$L_r = L_i - H \cot \alpha + \frac{L_{ref}}{2} \cdot \cos \alpha \tag{3}$$

$$l_r = L_r - L_{ref} \cdot \cos \beta \tag{4}$$

$$h_f = h_r - 5 \tag{5}$$

With H=15~mm, $L_{ref}=15~mm$, and $\beta=5^{\circ}$, Figure 4 displays the target geometries for the initial, reverse, and final passes. The outcome of the part formed through the localized reforming process is compared with a pyramid formed to the same target geometry in a single pass. In this context, a "pass" refers to the process of the tool traversing the workpiece, deforming it according to the toolpath generated by the software developed by Kiridena et al. [9].

Forming the material using the generated toolpath for the localized reforming process can lead to two defects in the final part, i.e., ruptures at the corners of the pyramid and wall protrusions. Corner ruptures occur when the tools start the reverse pass deformation at point B (Figure 5a), equivalent to a vertical step of approximately 10 mm (i.e., the distance between points B and D). To address this, the reverse pass is performed in four consecutive passes using three intermediate geometries, starting from point D, as shown in Figure 5a. Wall protrusion occurs when the hemispherical tip of the support tool contacts the pyramid walls at the start of the reverse pass around point B, causing unintended plastic deformation in the wall, as illustrated in Figure 5b.

To resolve this issue, any tool position with X and/or Y coordinates for the center of the hemispherical tool greater than $L_r - R$ in the reverse pass is adjusted to $L_r - R$.

Another parameter employed to enhance martensite transformation is the feedrate. In the localized reforming toolpath, a reduced feedrate of 500 mm/min is applied when the tools contact the region of interest (i.e., the area indicated by the red color in Figure 4) to reduce the heating effect, while a feedrate of 3000 mm/min is used elsewhere. In the single pass case, a feedrate of 3000 mm/min is used throughout the entire toolpath.

A bidirectional z-level toolpath with a 0.1 mm step-down is used as the toolpath type. The gap between the tools is calculated using the sine law and is defined as the squeeze factor, which is set as 0.95 for the initial and final passes and 0.98 for the reverse pass. This adjustment is made to avoid a sharp bending angle at the beginning of the reverse pass, which could cause defects on the final part, e.g., tearing. In the case of the single pass, a squeeze factor of 0.95 is employed. Super Lube Translucent Multi-Purpose Synthetic Lubricant with Syncolon (PTFE) is thoroughly applied to both sides of the sheet before each forming pass to prevent its removal by the tools. The emissivity value is assumed to remain constant throughout the forming process. A summary of the experimental parameters can be found in Table 1.

3. Finite element model for simulation

The effect of the deformation path in the single pass and localized reforming toolpaths is studied through FE simulations employing ABAQUS/Explicit software. The blank is constructed with 35,132 linear brick elements with reduced integration (C3D8R) and a finer mesh design (1 x 1 x 0.4 mm³) is considered in the central forming region. Note that a greater number of elements through-thickness to enhance the

accuracy of FE simulations would be required if exact predictions of, e.g., strain, are desired, but this would increase the computation time considerably. The focus of this study is to compare the DSIF results under two different toolpaths rather than striving for precise predictions for each of them, and thus only three elements through the thickness are used.

In addition, simple isotropic material properties are assumed, incorporating J2-plasticity and the Hockett-Sherby hardening law, which is expressed as $\bar{\sigma}=2089-1799\cdot \exp(-0.95\bar{\epsilon}^{0.72})$ (MPa) to reduce the computational load by avoiding complicated material modeling approach [4,43]. The parameters of the Hockett-Sherby hardening law are determined based on uniaxial tension stress-strain results. These tests, conducted with three repetitions at room temperature in the rolling direction, use prescribed displacement rates according to ISO 6892-1, producing a strain rate of ~0.001 s⁻¹.

The same toolpaths as the experiment are applied to the rigid tool holders (see Figure 6), which are connected to tool shanks and rigid hemispherical tooltips on each side of the sheet. This is to consider the tool deflection [22], which increases the gap between the two tools causing the sheet to deform with a lower squeeze factor. To incorporate the tool deflection in the simulation, the tool geometry is simplified into three sections: a rigid tip, deformable shank, and rigid holder, as shown in Figure 6. The tooltip is constructed using rigid elements maintaining the same 10 mm hemisphere geometry as in the experiments. In contrast, the tool shank is modeled as a cylindrical deformable body using 43 equal-length beam elements (B31), defined by Hooke's law (E=200 GPa, ν =0.33) since only elastic deformation exists due to the relatively low bending forces exerted. The 9.2 mm radius is determined by the Euler–Bernoulli beam theory for cantilever beam deflection under a point load, maintaining

equivalence of bending moments to the original tool shape. Then, the top of the deformable shank is connected to the rigid tool holder where the toolpath's boundary conditions are applied. A Coulomb friction model, with a constant coefficient of friction (μ =0.1) between the tooltip and sheet surfaces, is adopted. It is important to highlight that no contact is specified between the tool shank and the sheet in the numerical model; hence, the tool shank does not contact the sheet in the simulation.

To reduce the computational cost, artificial time scaling is employed. Scaling factors of 100 for the straight toolpath and 70 for the corners of the pyramid geometry are utilized, ensuring that the ratio of kinetic energy to internal energy remains below 5%. It is noteworthy that mass scaling is not used in this study because artificially increasing the mass of the tools leads to excessive tool deflection due to centrifugal forces rather than forming forces. The simulations are conducted utilizing 32 CPU cores, with a total wall clock time of 16 days for the single pass case and 27 days for the localized reforming toolpath. Moreover, an additional step utilizing ABAQUS/Standard is incorporated to capture springback after the removal of the tools and boundary conditions, which is equivalent to unloading the deformed sample from the fixture.

4. Experimental results and discussion

Figure 7 shows the specimens formed using the single pass and localized reforming (after each pass) toolpaths. To investigate the impact of the localized reforming toolpath on deformation-induced martensite transformation, the martensite fraction of formed parts using the single pass case and each pass of the localized reforming toolpath is measured at four locations along the wall. Figure 8 illustrates these measurement points on the specimens. Note that Locations 1 to 4 are different

from the points A-D in Figure 3. Measurement points on the specimen formed by the single pass case are the same as the final pass of the localized reforming toolpath, shown in Figure 8c. The distance between adjacent locations is 10 mm along the wall surface. Measurement of the martensite fraction at each of these points is obtained using an FMP30C Feritscope, which is a non-destructive method that relies on the magnetic permeability of the martensite phase. Mamros et al. [44] demonstrated that the readings from this device correspond to Electron Backscatter Diffraction (EBSD) measurements for SS304. Note that the reverse forming area is large enough (length along the wall >10 mm) to ensure that the remaining area without reforming does not influence the Feritscope measurements.

Figure 9 presents the martensite fraction at each measurement location for the single pass case and every pass of the localized reforming toolpath. The symbols in this figure represent the average of five readings at each measurement location, where the error bars are the maximum and minimum values of these measurements. The maximum standard deviation of a given measurement location is 1.2. The changes in martensite transformation can be attributed to both the accumulated plastic deformation and temperature change. Figure 10 displays the equivalent plastic strain evolution at each measurement location during single pass case and different passes of the localized reforming toolpath obtained from the FE simulations. Figure 11 illustrates the temperature contours for each measurement location during plastic deformation in both single pass and reforming toolpaths. The cells labeled "No plastic deformation" in this figure indicate that the corresponding measurement location is not plastically deformed by the tools at this location and for this particular pass.

During the initial pass of localized reforming, Locations 1, 2, and 3 experience plastic deformation, as evidenced by their equivalent plastic strain evolution in Figure

10a (represented by red, green, and blue dense-dashed lines, respectively). This leads to martensite fractions of 22%, 9.2%, and less than 5%, respectively, as shown in Figure 9. The decreasing martensite fraction is due to the accumulated heat generated by plastic deformation (temperature increase from ~55°C at Location 1 to ~77°C at Location 3), as shown in Figure 11. Following the reverse pass, there is a significant increase in martensite transformation at Location 3, rising to 28.5%. This increase aligns with the increased plastic deformation ($\Delta \bar{\epsilon}$ =0.12, blue dashed line in Figure 10a) and lowered temperature (~31°C in Figure 11) during the reverse pass. In contrast to Location 3, the other locations remain relatively unaffected during this pass.

During the final pass of localized reforming, Location 3 undergoes a substantial increase in plastic deformation ($\Delta \bar{\varepsilon} = 0.17$), reaching 68.4% martensite fraction. Similarly, Locations 2 and 4 obtain additional plastic deformation ($\Delta \bar{\varepsilon}$ =0.03 and 0.50, respectively), reaching 26% and 24.3% martensite fraction, respectively, while Location 1 does not experience any plastic deformation during the final pass. (The relatively low martensite fraction, compared to the plastic deformation, achieved at Location 4 will be explained with the temperature effect later.) These results demonstrate that the localized reforming path successfully increases the martensite fraction in the region of interest, i.e., Location 3. The single pass simulation results in Figure 10b show that nearly the same strain values with the localized reforming toolpath are induced at Locations 1, 2, and 4 compared to the localized reforming toolpath (the maximum difference being 0.04 difference at Location 4, which will be explained later in the paper in the thickness distribution analysis). The only significant variation in strain values occurs at Location 3, i.e., $\bar{\varepsilon}$ =0.54 for the single pass case versus $\bar{\varepsilon}$ =0.84 for the localized reforming toolpath due to the additional deformation being induced. Additionally, a 0.03 difference in strain is seen at Location 2 ($\bar{\varepsilon}$ =0.33 for the single pass case versus $\bar{\varepsilon}$ =0.36 for the localized reforming toolpath) due to some deformation ($\Delta \bar{\varepsilon}$ =0.03) generated during the reverse pass.

In the single pass case, Locations 1 and 2 experience a similar increase in transformation as in the initial pass of localized reforming, while Locations 3 and 4 show minor amounts of transformation. Again, the decreasing trend of the martensite fraction from Location 1 to Location 4 in the single pass case is due to the increase in the temperature (from ~55°C at Location 1 to ~81°C at Location 4, as shown in Figure 11).

Further analysis of the temperature results reveals that the material plastically deforms at lower temperatures at Locations 2 and 3 in the reverse and final passes of the localized reforming toolpath. This is mainly caused by higher heat dissipation due to the lower feedrate and interruptions between each pass of the localized reforming. The lower forming temperature at Location 3 in the reverse pass, i.e., ~31°C (compared to ~77°C in the initial pass) explains the higher transformation (28.5%, compared to <5% in the initial pass) despite the lower plastic deformation increment $(\Delta \bar{\varepsilon}=0.55)$ in the initial pass, compared to 0.12 in the reforming pass). Moreover, a higher transformation is observed at Location 4 during the final pass of the localized reforming toolpath compared to the single pass case (24.3% compared to 5.2%) while in both cases this measurement point is deformed only once. This is due to the lower deformation temperature in the localized reforming deformation path (~62°C) compared to the single pass case (~81°C). Furthermore, a relatively similar martensite fraction is observed at Locations 2 and 4 (26% and 24.3%, respectively) after the final pass of the localized reforming toolpath, despite Location 4 exhibiting higher final plastic strain than Location 2 ($\bar{\varepsilon}$ =0.55 compared to 0.36). This is attributed to the lower temperatures at the moment of plastic deformation at Location 2 compared to Location

4 (~26°C compared to ~62°C) during the final pass of the localized reforming toolpath.

A summary of the experimental (temperature and martensite transformation) and numerical (final equivalent plastic strain) results can be found in Table 2 in Appendix A.1.

In addition to evaluating martensite transformation, the cross-sectional profiles of the truncated pyramids are examined. After each pass of the localized reforming process, as well as in the single pass case, the specimens are unclamped and scanned using a Faro Arm Quantum laser line probe, which has an accuracy specification of ±0.025 mm. Figure 12 displays the profiles of the specimens after single pass case and each pass of the localized reforming toolpath, with martensite measurement locations indicated. Additionally, Figure 12 presents simulation predictions of the cross-sectional profile for both the single pass and the final pass of localized reforming toolpaths, which are nearly identical. A comparison between the experimental results of single pass and localized reforming toolpaths reveals that both cases are formed to nearly the same geometry. This illustrates that the localized reforming successfully maintains geometric accuracy while the increased martensite transformation is achieved in the region of interest. The predicted profile from the simulation is in good agreement with the experiments; however, a minor deviation exists at the center of the inclined wall of the pyramid in the localized reforming toolpath (between solid red and green lines shown in the insets of Figure 12). The error in the prediction is possibly caused by the simplifications in the model, e.g., not considering the generated heat during deformation, martensite transformation kinetics [45–47], material anisotropy, etc.

The reverse pass profile displays a pronounced pillowing effect at the apex of the pyramid, which is a result of compressive forces acting in the plane of the sheet [48].

The reverse pass causes a slight change in the wall angle at Location 2, as it is close to the start point of the bending region of the reverse pass (shown in the inset in Figure 12). Recall that, since the final pass of localized reforming starts from point A in Figure 3, any geometrical variation due to bending during the reverse pass should be corrected in the final pass, as evidenced by a marginal strain increment ($\Delta \bar{\varepsilon}$ =0.03) at the onset of the final pass in Figure 10a (green solid line).

Following the profile scanning, the parts are cut in half perpendicular to the rolling direction to measure the thickness along the cross-section using a micrometer. The values at each measurement location are averaged and the results of both toolpaths are presented in Figure 13 along with the simulation predictions. Both toolpaths show a similar thickness distribution from the base of the pyramid to Location 2, but the localized reforming toolpath starts deviating with slightly lower thickness at Location 3 and greater around Location 4. Location 3 undergoes plastic deformation in the initial, reverse, and final passes, which leads to higher thinning compared to the single pass case. For Location 4, the material undergoes forming once in both deformation paths. However, the relatively lower temperature in the localized reforming toolpath (~62°C) can reduce the thermal softening and thinning at Location 4 compared to the single pass case (~81°C). Additionally, the parallel wall angle to the target geometry at Location 4 after the reverse pass (circled triangle symbol in Figure 12) requires less change during the final pass compared to the single pass case. This can be observed by slightly lower plastic deformation experienced by Location 4 during the localized reforming toolpath compared to the single pass case, with $\bar{\varepsilon}$ =0.55 and 0.59, respectively, as shown in Figures 10a and 10b.

While the FE simulation prediction aligns well with the experimental results, e.g., for the single pass case, it predicts less thinning than observed experimentally near

Location 2 and near the corner of the pyramid apex for the localized reforming toolpath. This discrepancy may arise due to not accounting for the martensite transformation kinetics in the simulations, especially at Locations 2 and 3 experiencing the reverse loading and thus the Bauschinger effect, but much more critical at Location 2 which is close to the bending region of the reverse pass. In the single pass case, where there is lower martensite transformation and no reverse pass, more accurate thickness predictions are achieved despite the absence of transformation kinetics and temperature in the model.

6. Conclusions and summary

In this paper, the capability of the DSIF process to locally manipulate the deformation-induced martensite transformation by using a localized reforming toolpath and varying the feedrate is demonstrated. This is evaluated by comparing the martensite fraction, geometrical accuracy, and thickness distribution of truncated pyramids formed by a localized reforming toolpath and a conventional single pass case. Moreover, FE simulations are used to explain the effect of the reverse pass on plastic deformation and its relation to the martensite transformation. It is observed that implementing a reverse forming pass at the desired region of the pyramid wall resulted in an accumulation of plastic deformation and thus a localized increase in the martensite fraction leading to higher strength. Geometrical accuracy and thickness distribution remain comparable to those in a single pass case. Measurements of martensite transformation indicate that achieving transformations as high as ~70% at the region of interest, i.e., the center of the pyramid wall, is feasible while the martensite transformation at other locations along the wall remains lower, around 25%. In contrast, the maximum martensite fraction with a single pass case is 20%, with a

decreasing trend from the base to the apex due to the temperature increase during the forming process. These findings underscore the potential to tailor mechanical properties in specific regions of interest by employing a localized reforming toolpath in the DSIF process. This methodology holds promise for producing, e.g., trauma fixation hardware with heterogeneous mechanical properties, exemplified by cranial implants with enhanced strength at the mounting regions, while maintaining a lightweight and formable structure elsewhere.

Acknowledgements

Funding for the NH BioMade Project from the U.S. National Science Foundation EPSCoR award (#1757371).

Appendix

A.1 Experimental and numerical results summary

A summary of the experimental (temperature and martensite transformation) and numerical (final equivalent plastic strain) results at each of the measurement locations (i.e., Locations 1-4) during single pass toolpath and every pass of the localized reforming case are shown in Table 2.

References

- [1] Jeswiet, J., Micari, F., Hirt, G., Bramley, A., Duflou, J., and Allwood, J., 2005, "Asymmetric Single Point Incremental Forming of Sheet Metal," CIRP Annals, **54**(2), pp. 88–114.
- [2] Chen, K., Breunig, A., Ha, J., Kinsey, B. L., Groche, P., and Korkolis, Y. P., 2022, "Robustness of Deep-Drawing Finite-Element Simulations to Process Variations," Int J Mater Form, **15**(3), p. 45.
- [3] Groche, P., Breunig, A., Chen, K., Molitor, D. A., Ha, J., Kinsey, B. L., and Korkolis, Y. P., 2022, "Effectiveness of Different Closed-Loop Control Strategies for Deep Drawing on Single-Acting 3D Servo Presses," CIRP Annals, **71**(1), pp. 357–360.
- [4] Ha, J., Fones, J., Kinsey, B. L., and Korkolis, Y. P., 2020, "Plasticity and Formability of Annealed, Commercially-Pure Aluminum: Experiments and Modeling," Materials, 13(19), p. 4285.
- [5] Ha, J., Coppieters, S., and Korkolis, Y. P., 2020, "On the Expansion of a Circular Hole in an Orthotropic Elastoplastic Thin Sheet," International Journal of Mechanical Sciences, **182**, p. 105706.
- [6] Ha, J., and Korkolis, Y. P., 2021, "Hole-Expansion: Sensitivity of Failure Prediction on Plastic Anisotropy Modeling," Journal of Manufacturing and Materials Processing, 5(2), p. 28.
- [7] Kumar, S. P., Elangovan, S., Mohanraj, R., and Boopathi, S., 2021, "Real-Time Applications and Novel Manufacturing Strategies of Incremental Forming: An Industrial Perspective," Materials Today: Proceedings, **46**, pp. 8153–8164.
- [8] Gupta, P., Szekeres, A., and Jeswiet, J., 2019, "Design and Development of an Aerospace Component with Single-Point Incremental Forming," Int J Adv Manuf Technol, **103**(9), pp. 3683–3702.
- [9] Kiridena, V., Verma, R., Gutowski, T., and Roth, J., 2018, *Rapid Freeform Sheet Metal Forming: Technology Development and System Verification*, DOE-FORD-05764-1, Ford Motor Company, Detroit, MI (United States).
- [10] Scheffler, S., Pierer, A., Scholz, P., Melzer, S., Weise, D., and Rambousek, Z., 2019, "Incremental Sheet Metal Forming on the Example of Car Exterior Skin Parts," Procedia Manufacturing, **29**, pp. 105–111.

- [11] Lu, B., Ou, H., Shi, S. Q., Long, H., and Chen, J., 2016, "Titanium Based Cranial Reconstruction Using Incremental Sheet Forming," Int J Mater Form, 9(3), pp. 361–370.
- [12] Duflou, J. R., Habraken, A.-M., Cao, J., Malhotra, R., Bambach, M., Adams, D., Vanhove, H., Mohammadi, A., and Jeswiet, J., 2018, "Single Point Incremental Forming: State-of-the-Art and Prospects," Int J Mater Form, **11**(6), pp. 743–773.
- [13] McAnulty, T., Jeswiet, J., and Doolan, M., 2017, "Formability in Single Point Incremental Forming: A Comparative Analysis of the State of the Art," CIRP Journal of Manufacturing Science and Technology, **16**, pp. 43–54.
- [14] Golabi, S., and Khazaali, H., 2014, "Determining Frustum Depth of 304 Stainless Steel Plates with Various Diameters and Thicknesses by Incremental Forming," J Mech Sci Technol, **28**(8), pp. 3273–3278.
- [15] Darzi, S., Mirnia, M. J., and Elyasi, M., 2021, "Single-Point Incremental Forming of AA6061 Aluminum Alloy at Elevated Temperatures," Int J Adv Manuf Technol, **116**(3), pp. 1023–1039.
- [16] Silva, M. B., and Martins, P. A. F., 2013, "Two-Point Incremental Forming with Partial Die: Theory and Experimentation," J. of Materi Eng and Perform, **22**(4), pp. 1018–1027.
- [17] Boudhaouia, S., Gahbiche, M. A., Ayed, Y., Giraud, E., Ben Salem, W., and Dal Santo, P., 2018, "Experimental and Numerical Study of a New Hybrid Process: Multi-Point Incremental Forming (MPIF)," Int J Mater Form, 11(6), pp. 815–827.
- [18] Maidagan, E., Zettler, J., Bambach, M., Rodríguez, P. P., and Hirt, G., 2007, "A New Incremental Sheet Forming Process Based on a Flexible Supporting Die System," Key Engineering Materials, **344**, pp. 607–614.
- [19] Peng, W., Ou, H., and Becker, A., 2019, "Double-Sided Incremental Forming: A Review," Journal of Manufacturing Science and Engineering, **141**(5).
- [20] Ai, S., and Long, H., 2019, "A Review on Material Fracture Mechanism in Incremental Sheet Forming," Int J Adv Manuf Technol, **104**(1), pp. 33–61.
- [21] Maqbool, F., and Bambach, M., 2018, "Dominant Deformation Mechanisms in Single Point Incremental Forming (SPIF) and Their Effect on Geometrical Accuracy," International Journal of Mechanical Sciences, **136**, pp. 279–292.
- [22] Darzi, S., Kinsey, B. L., and Ha, J., 2024, "Reforming Toolpath Effect on Deformation Mechanics in Double-Sided Incremental Forming," International Journal of Mechanical Sciences, **280**, p. 109548.
- [23] Malhotra, R., Cao, J., Ren, F., Kiridena, V., Cedric Xia, Z., and Reddy, N. V., 2011, "Improvement of Geometric Accuracy in Incremental Forming by Using a Squeezing Toolpath Strategy With Two Forming Tools," Journal of Manufacturing Science and Engineering, 133(6).
- [24] Peng, W., and Ou, H., 2023, "Deformation Mechanisms and Fracture in Tension under Cyclic Bending plus Compression, Single Point and Double-Sided Incremental Sheet Forming Processes," International Journal of Machine Tools and Manufacture, **184**, p. 103980.
- [25] Smith, J., Malhotra, R., Liu, W. K., and Cao, J., 2013, "Deformation Mechanics in Single-Point and Accumulative Double-Sided Incremental Forming," Int J Adv Manuf Technol, **69**(5), pp. 1185–1201.
- [26] Wang, H., Zhang, R., Zhang, H., Hu, Q., and Chen, J., 2018, "Novel Strategies to Reduce the Springback for Double-Sided Incremental Forming," Int J Adv Manuf Technol, 96(1), pp. 973–979.

- [27] Lu, B., Fang, Y., Xu, D. K., Chen, J., Ai, S., Long, H., Ou, H., and Cao, J., 2015, "Investigation of Material Deformation Mechanism in Double Side Incremental Sheet Forming," International Journal of Machine Tools and Manufacture, **93**, pp. 37–48.
- [28] Junchao, L., Junjian, S., and Bin, W., 2013, "A Multipass Incremental Sheet Forming Strategy of a Car Taillight Bracket," Int J Adv Manuf Technol, **69**(9), pp. 2229–2236.
- [29] Moser, N., Ndip-Agbor, E., Ren, H. Q., Zhang, Z. X., Ehmann, K., and Cao, J., 2015, "Challenges and Process Strategies Concerning Multi-Pass Double Sided Incremental Forming," Key Engineering Materials, **651–653**, pp. 1122–1127.
- [30] Tekkaya, A. E., Groche, P., Kinsey, B. L., and Wang, Z. G., 2023, "Stress Superposition in Metal Forming," CIRP Annals.
- [31] Olson, G. B., and Cohen, M., 1975, "Kinetics of Strain-Induced Martensitic Nucleation," Metall Trans A, **6**(4), pp. 791–795.
- [32] Beese, A. M., and Mohr, D., 2011, "Effect of Stress Triaxiality and Lode Angle on the Kinetics of Strain-Induced Austenite-to-Martensite Transformation," Acta Materialia, **59**(7), pp. 2589–2600.
- [33] Kim, H., Lee, J., Barlat, F., Kim, D., and Lee, M.-G., 2015, "Experiment and Modeling to Investigate the Effect of Stress State, Strain and Temperature on Martensitic Phase Transformation in TRIP-Assisted Steel," Acta Materialia, **97**, pp. 435–444.
- [34] Wang, Z., and Beese, A. M., 2019, "Stress State-Dependent Mechanics of Additively Manufactured 304L Stainless Steel: Part 1 Characterization and Modeling of the Effect of Stress State and Texture on Microstructural Evolution," Materials Science and Engineering: A, 743, pp. 811–823.
- [35] DeMania, D. A., 1995, "The Influence of Martensitic Transformation on the Formability of 304L Stainless Steel Sheet," Thesis, Massachusetts Institute of Technology.
- [36] Hecker, S. S., Stout, M. G., Staudhammer, K. P., and Smith, J. L., 1982, "Effects of Strain State and Strain Rate on Deformation-Induced Transformation in 304 Stainless Steel: Part I. Magnetic Measurements and Mechanical Behavior," Metall Mater Trans A, 13(4), pp. 619–626.
- [37] Feng, Z., Mamros, E. M., Ha, J., Kinsey, B. L., and Knezevic, M., 2021, "Modeling of Plasticity-Induced Martensitic Transformation to Achieve Hierarchical, Heterogeneous, and Tailored Microstructures in Stainless Steels," CIRP Journal of Manufacturing Science and Technology, **33**, pp. 389–397.
- [38] Mamros, E. M., Bram Kuijer, M., Davarpanah, M. A., Baker, I., and Kinsey, B. L., 2021, "The Effect of Temperature on the Strain-Induced Austenite to Martensite Transformation in SS 316L During Uniaxial Tension," Forming the Future, G. Daehn, J. Cao, B. Kinsey, E. Tekkaya, A. Vivek, and Y. Yoshida, eds., Springer International Publishing, Cham, pp. 1853–1862.
- [39] Mamros, E. M., Mayer, S. M., Banerjee, D. K., Iadicola, M. A., Kinsey, B. L., and Ha, J., 2022, "Plastic Anisotropy Evolution of SS316L and Modeling for Novel Cruciform Specimen," International Journal of Mechanical Sciences, **234**, p. 107663.
- [40] Katajarinne, T., Louhenkilpi, S., and Kivivuori, S., 2014, "A Novel Approach to Control the Properties of Austenitic Stainless Steels in Incremental Forming," Materials Science and Engineering: A, **604**, pp. 23–26.
- [41] Mamros, E. M., Maaß, F., Hahn, M., Tekkaya, A. E., Ha, J., and Kinsey, B. L., 2022, "Superposing Tensile Stresses into Single Point Incremental Forming to Affect Martensitic Transformation of SS304," IOP Conf. Ser.: Mater. Sci. Eng., 1238(1), p. 012085.

- [42] Darzi, S., Adams, M. D., Roth, J. T., Kinsey, B. L., and Ha, J., 2023, "Manipulating Martensite Transformation of SS304L during Double-Sided Incremental Forming by Varying Temperature and Deformation Path," CIRP Annals, 72(1), pp. 221–224.
- [43] Kim, J., Pham, Q. T., Ha, J., and Kim, Y. S., 2022, "Constitutive Modeling of Commercial Pure Titanium Sheet Based on Non-Associated Flow Rule and Differential Hardening," International Journal of Mechanical Sciences, **230**, p. 107549.
- [44] Mamros, E. M., Polec, L. A., Maaß, F., Clausmeyer, T., Tekkaya, A. E., Ha, J., and Kinsey, B. L., 2024, "Examination of Bending Stress Superposition Effect on Martensite Transformation in Austenitic Stainless Steel 304," Proceedings of the 14th International Conference on the Technology of Plasticity Current Trends in the Technology of Plasticity, K. Mocellin, P.-O. Bouchard, R. Bigot, and T. Balan, eds., Springer Nature Switzerland, Cham, pp. 475–485.
- [45] Lee, J., Bong, H. J., Ha, J., Choi, J., Barlat, F., and Lee, M.-G., 2018, "Influence of Yield Stress Determination in Anisotropic Hardening Model on Springback Prediction in Dual-Phase Steel," JOM, **70**(8), pp. 1560–1566.
- [46] "Meso-Scopic Analysis of Strain Path Change Effect on the Hardening Behavior of Dual-Phase Steel Ha 2014 Steel Research International Wiley Online Library" [Online]. Available: https://onlinelibrary.wiley.com/doi/abs/10.1002/srin.201300186. [Accessed: 28-Feb-2024].
- [47] Ha, J., Lee, J., Kim, J. H., Lee, M.-G., and Barlat, F., 2017, "Investigation of Plastic Strain Rate under Strain Path Changes in Dual-Phase Steel Using Microstructure-Based Modeling," International Journal of Plasticity, 93, pp. 89–111.
- [48] Isidore, B. B. L., Hussain, G., Shamchi, S. P., and Khan, W. A., 2016, "Prediction and Control of Pillow Defect in Single Point Incremental Forming Using Numerical Simulations," J Mech Sci Technol, **30**(5), pp. 2151–2161.

Figure captions:

- Figure 1: Schematics of incremental forming variants: (a) SPIF, (b) TPIF, and (c) DSIF.
- **Figure 2:** Experimental setup: (a) DSIF machine and (b) tools and FLIR camera for temperature measurement.
- **Figure 3:** Parametric dimensions of (a) target geometry, (b) initial pass, and (c) reverse pass.
- Figure 4: Target geometries of (a) initial pass, (b) reverse pass, and (c) final pass.
- **Figure 5:** Reforming toolpath modifications: (a) adding intermediate geometries to reverse pass and (b) adjusting the position of tools.
- Figure 6: Schematic of FE simulation with blank mesh design and tool simplification.
- **Figure 7:** Formed specimens after single pass and localized reforming with (a) initial pass, (b) reverse pass, and (c) final pass.
- **Figure 8:** Martensite transformation measurement locations on reforming specimen after (a) initial pass, (b) reverse pass, and (c) final pass, as well as single pass case.
- **Figure 9:** Martensite fraction measurements after single pass and localized reforming toolpaths.
- **Figure 10:** Equivalent plastic strain evolution along the wall for (a) localized reforming passes and (b) single pass predicted by numerical simulations.
- **Figure 11:** Temperature contours for each measurement location while plastically deforming during single pass and localized reforming toolpaths. The values indicate the local temperatures at each location.
- **Figure 12:** Profile of specimens after single pass and each pass of localized reforming toolpaths: a comparison between experiments and simulation results.
- **Figure 13:** Thickness distribution of parts after single pass and final pass of localized reforming toolpaths, including a comparison between experiments and simulation results.

Table headings:

Table 1 Experimental parameters summary

Table 2 Experimental and numerical results summary



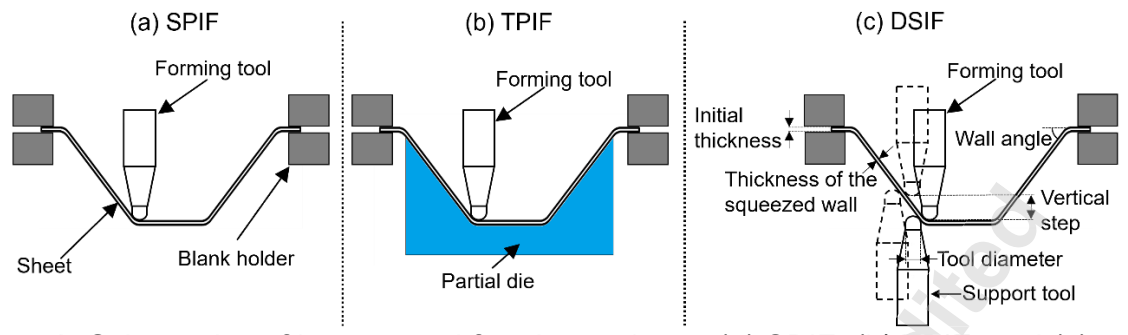


Figure 1: Schematics of incremental forming variants: (a) SPIF, (b) TPIF, and (c) DSIF.

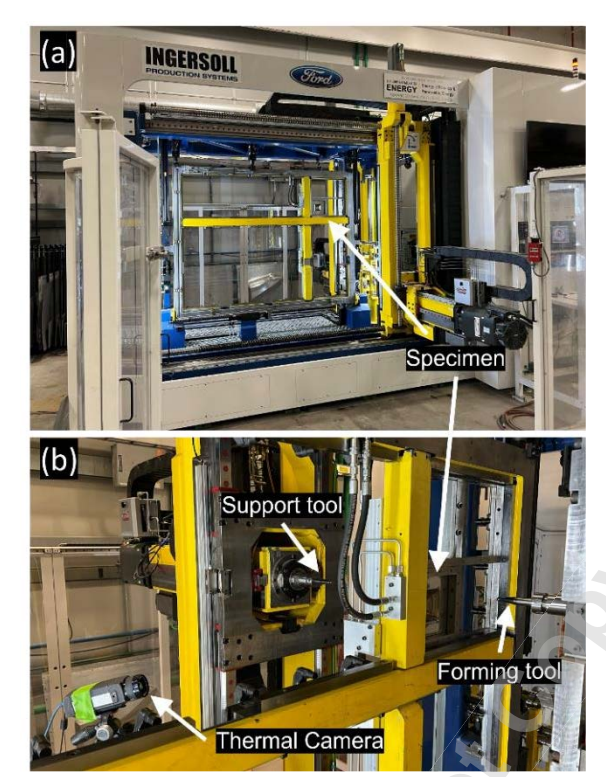


Figure 2: Experimental setup: (a) DSIF machine and (b) tools and FLIR camera for temperature measurement.

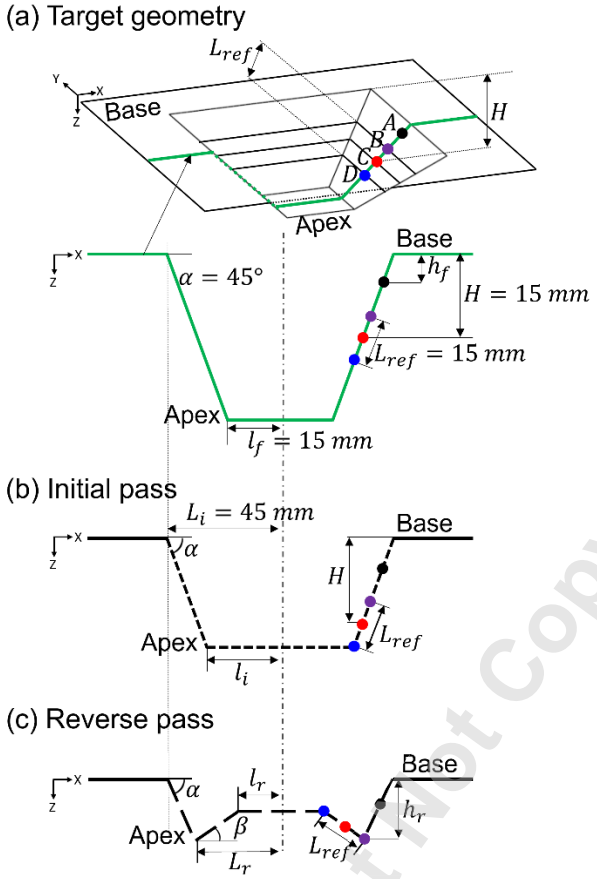


Figure 3: Parametric dimensions of (a) target geometry, (b) initial pass, and (c) reverse pass.

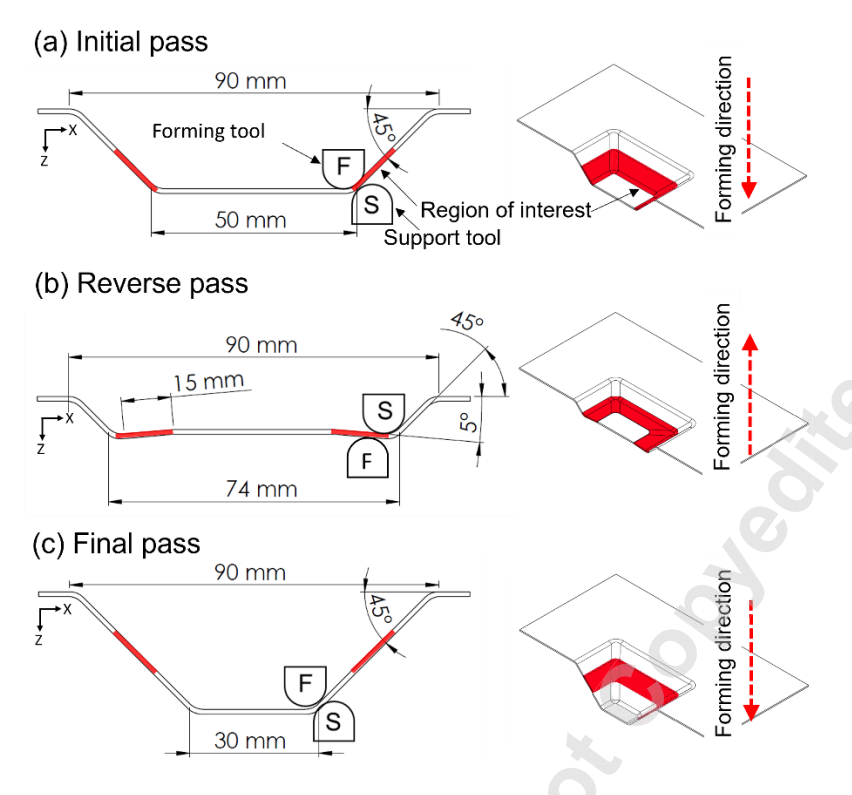


Figure 4: Target geometries of (a) initial pass, (b) reverse pass, and (c) final pass.

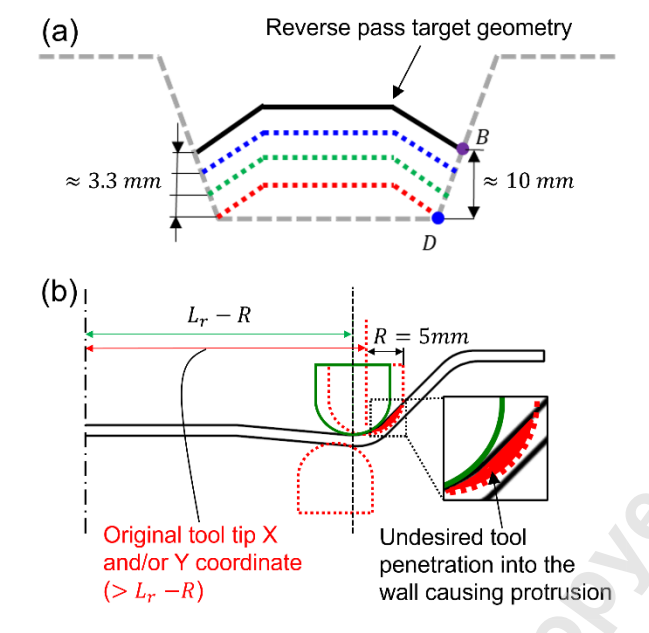


Figure 5: Reforming toolpath modifications: (a) adding intermediate geometries to reverse pass and (b) adjusting the position of tools.

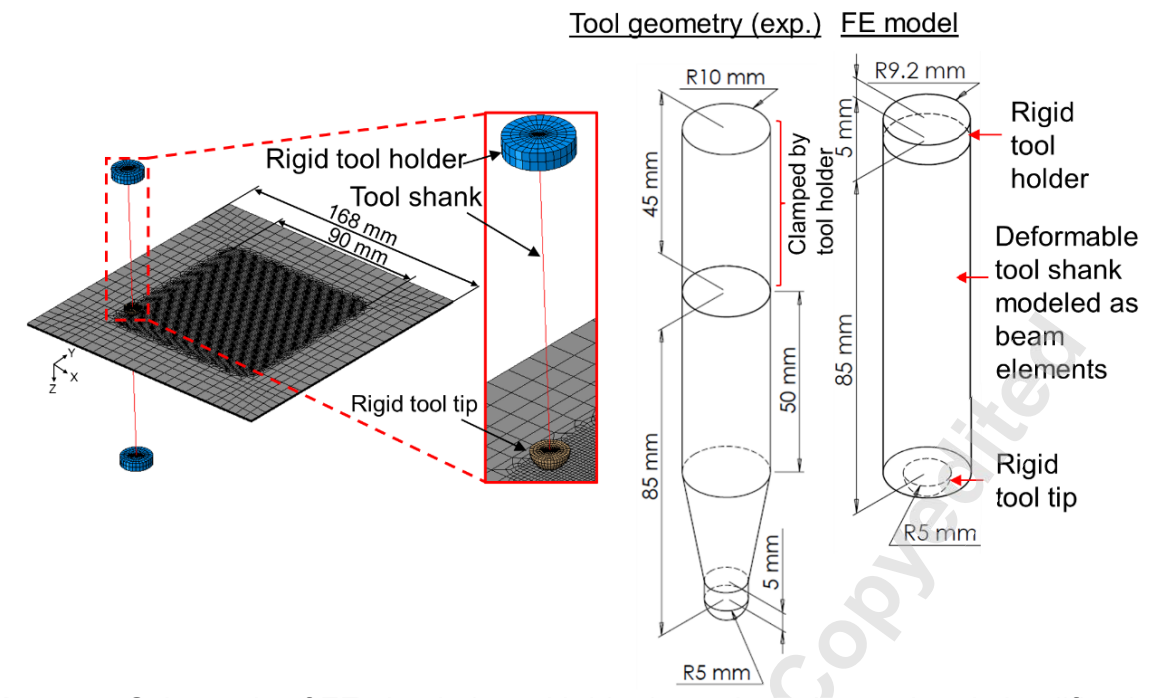


Figure 6: Schematic of FE simulation with blank mesh design and tool simplification.

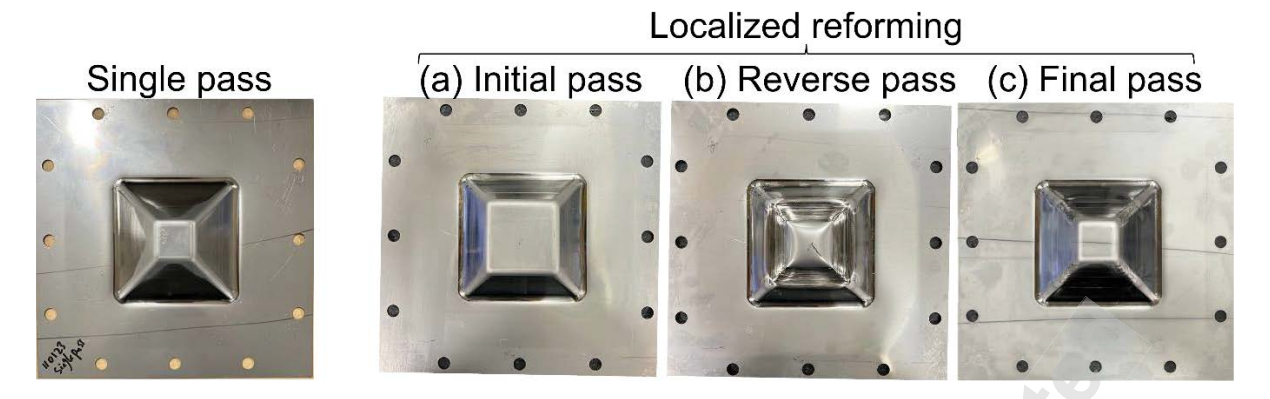


Figure 7: Formed specimens after single pass and localized reforming with (a) initial pass, (b) reverse pass, and (c) final pass.

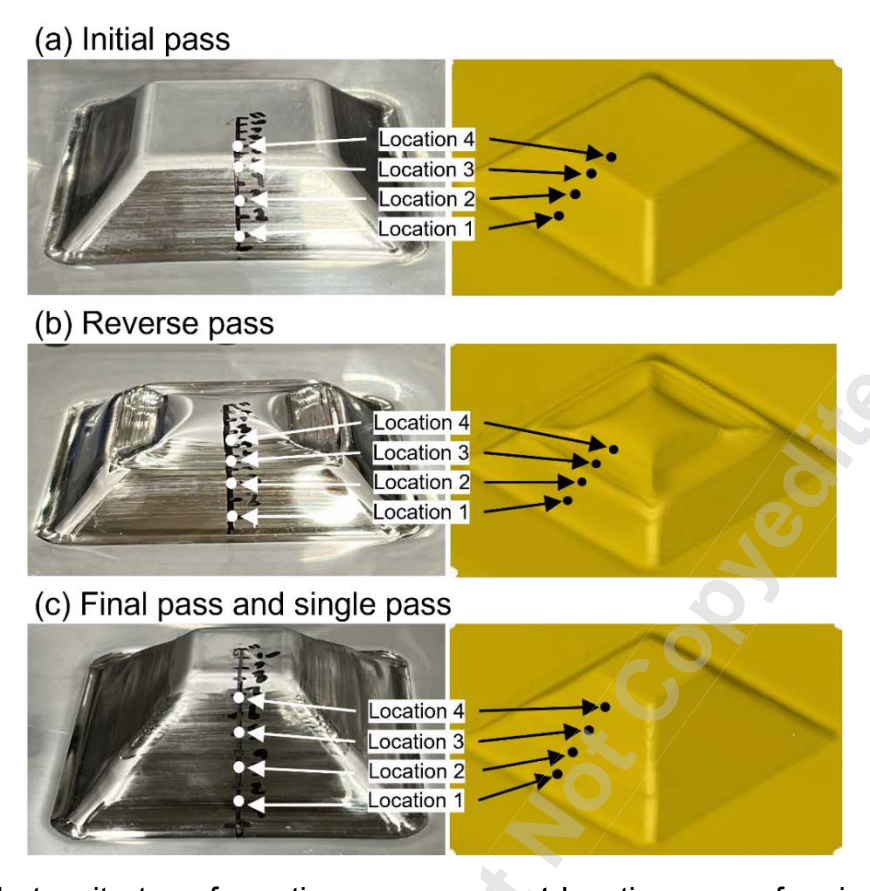


Figure 8: Martensite transformation measurement locations on reforming specimen after (a) initial pass, (b) reverse pass, and (c) final pass, as well as single pass case.

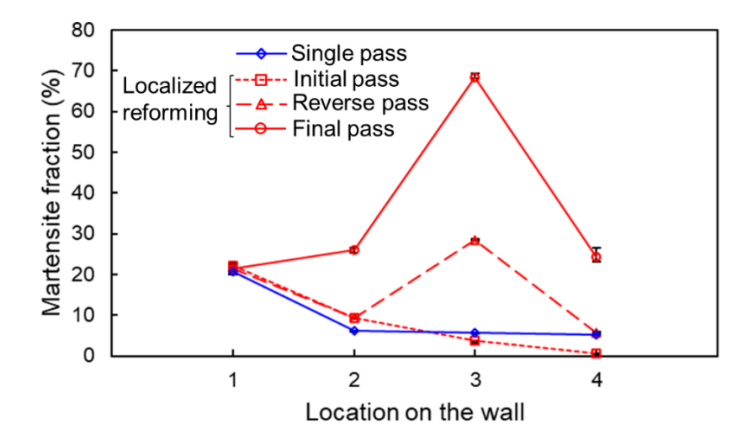


Figure 9: Martensite fraction measurements after single pass and localized reforming toolpaths.

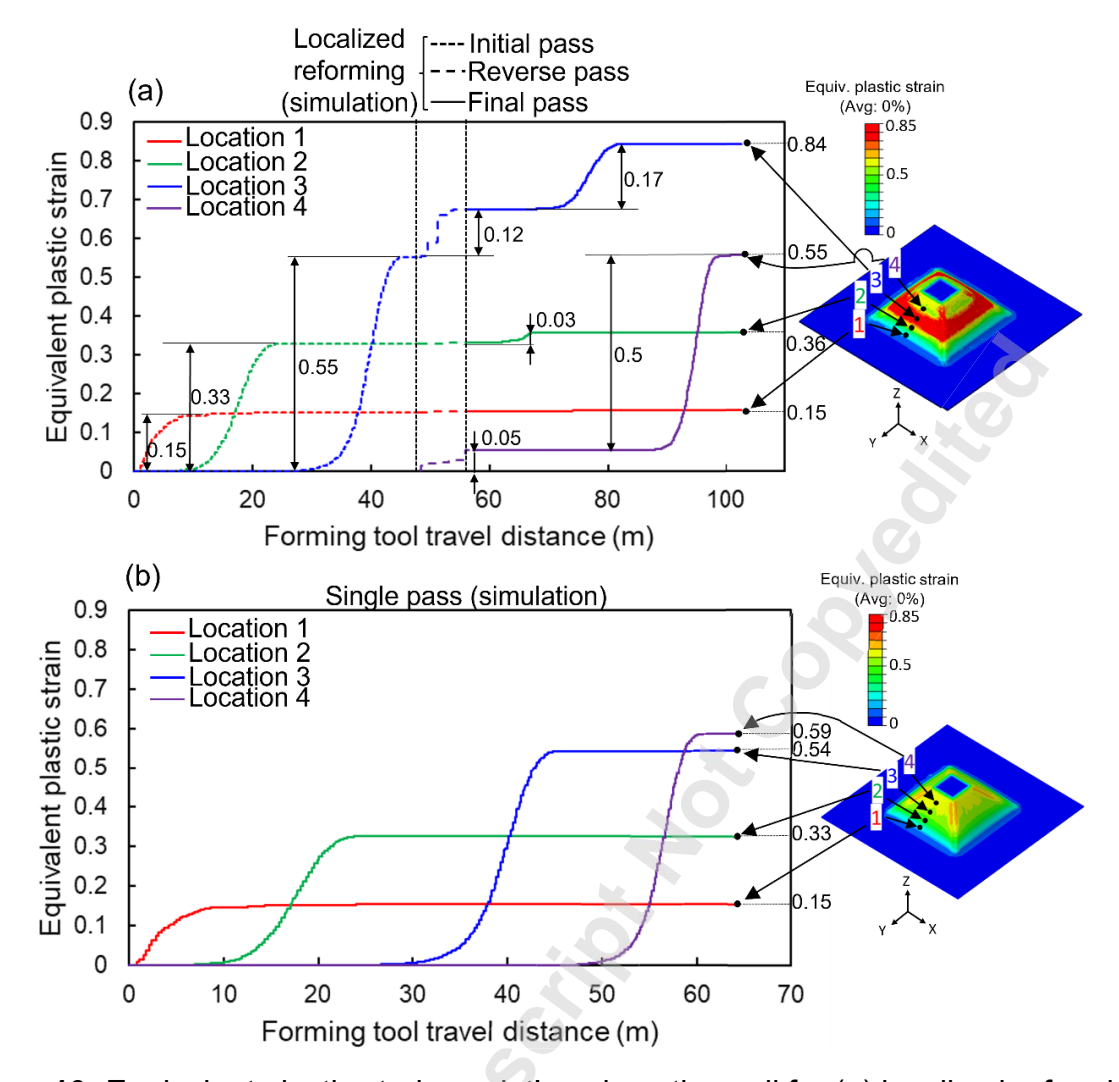


Figure 10: Equivalent plastic strain evolution along the wall for (a) localized reforming passes and (b) single pass predicted by numerical simulations.

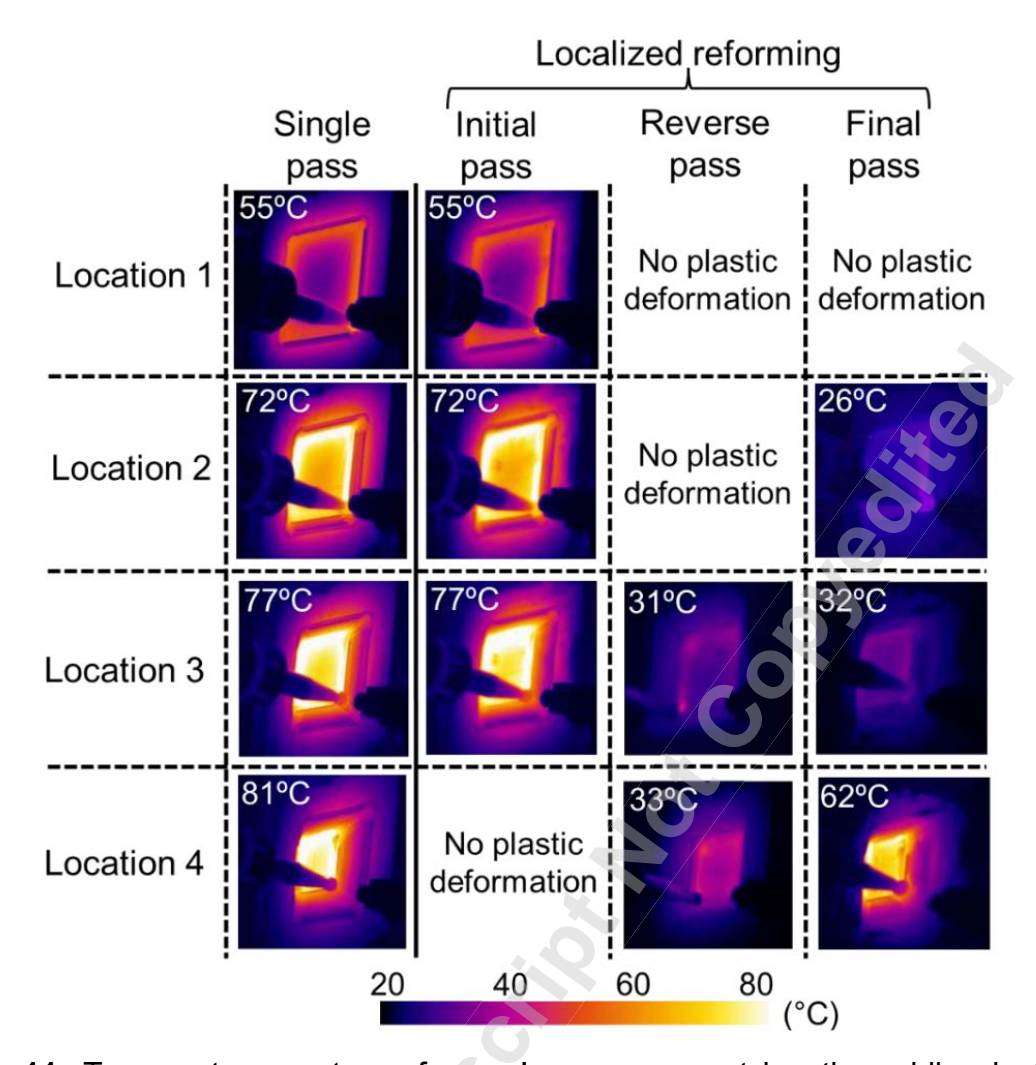


Figure 11: Temperature contours for each measurement location while plastically deforming during single pass and localized reforming toolpaths. The values indicate the local temperatures at each location.

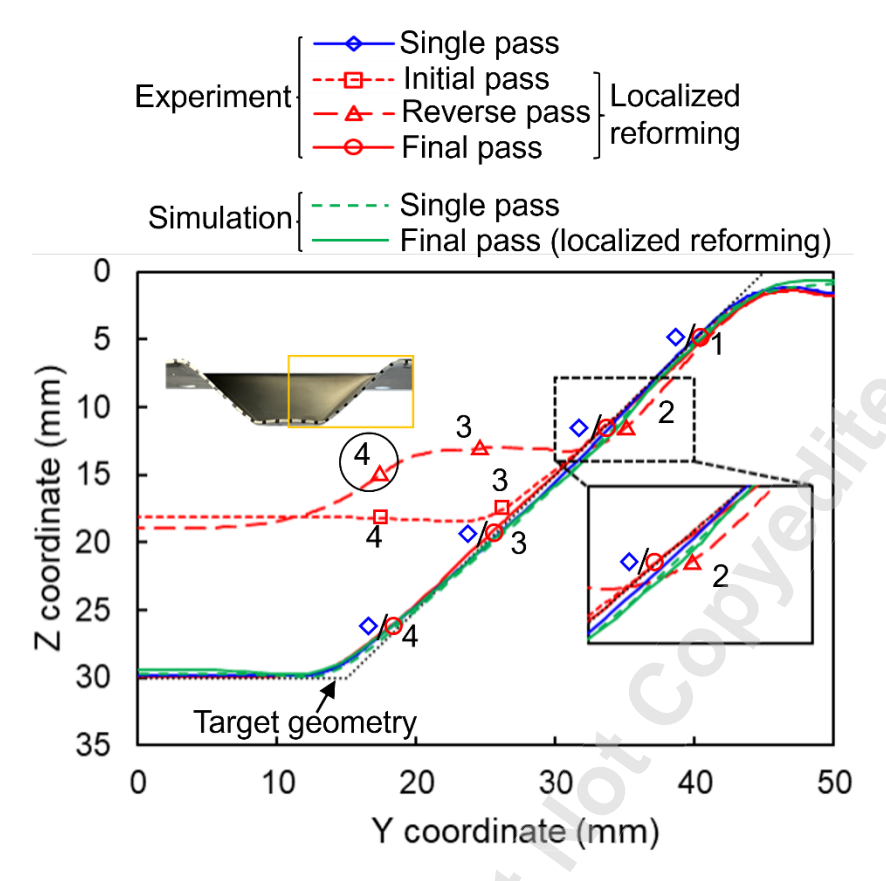


Figure 12: Profile of specimens after single pass and each pass of localized reforming toolpaths: a comparison between experiments and simulation results.

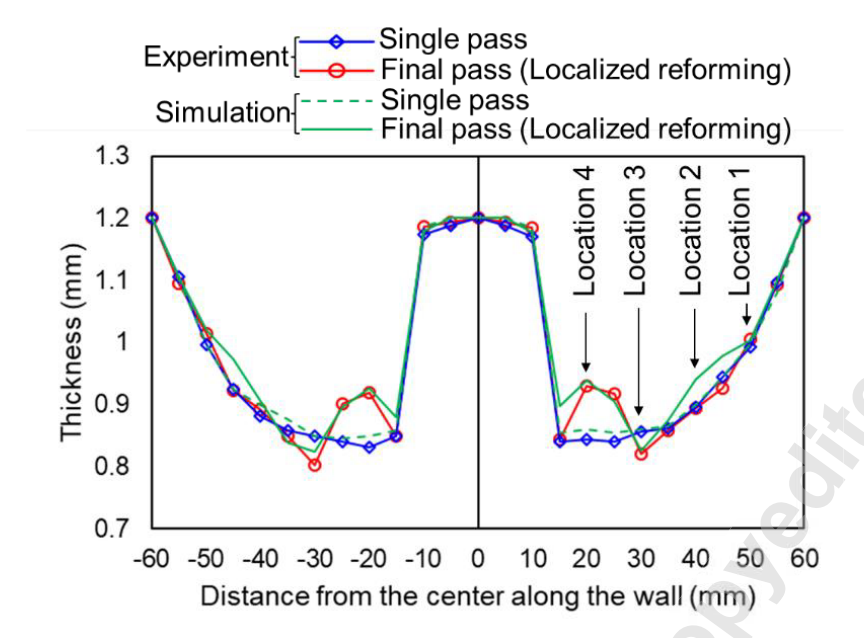


Figure 13: Thickness distribution of parts after single pass and final pass of localized reforming toolpaths, including a comparison between experiments and simulation results.

Table 1 Experimental parameters summary

Pass		Single				
Parameter	Initial pass	Reverse pass	Final pass	- Single pass		
Tool feedrate (mm/min)	3000	500	500 within the region of interest, 3000 elsewhere	3000		
Squeeze factor	0.95	0.98	0.95	0.95		
Tool-tip material and geometry A2 steel, 10 mm hemisphere (same			misphere (same for bo	th tools)		
Material and initial blank size	SS304 (215 mm×215 mm×1.2 mm)					
Lubricant	Multi-Purpose Synthetic Lubricant with Syncolon (PTFE)					
Toolpath technique	Standard bi-directional Z-level					

Table 2 Experimental and numerical results summary

Parameter	Temperature (°C)			Equivalent plastic strain			Martensite transformation (%)		
Location	Single pass	Localized reforming		Single pass	Localized reforming		Single pass	Localized reforming	
Location 1	55	Initial pass	55	0.15	Initial pass	0.15	20.7	Initial pass	22
		Reverse pass	NA		Reverse pass	0.15		Reverse pass	22
		Final pass	NA		Final pass	0.15		Final pass	22
Location 2	72	Initial pass	72	0.33	Initial pass	0.33	6.2	Initial pass	9.2
		Reverse pass	NA		Reverse pass	0.33		Reverse pass	9.2
		Final pass	26		Final pass	0.36		Final pass	26
Location 3	77	Initial pass	77	0.54	Initial pass	0.55	5.6	Initial pass	3.6
		Reverse pass	31		Reverse pass	0.67		Reverse pass	28.5
		Final pass	32		Final pass	0.84		Final pass	68.4
Location 4	81	Initial pass	NA	0.59	Initial pass	0	5.2	Initial pass	0.6
		Reverse pass	33		Reverse pass	0.05		Reverse pass	5.5
		Final pass	62		Final pass	0.55		Final pass	24.3